Nitrate radical generation via continuous generation of dinitrogen pentoxide in a laminar flow reactor coupled to an oxidation flow reactor

Andrew T. Lambe[1], Ezra C. Wood[2], Jordan E. Krechmer[1], Francesca Majluf[1], Leah R. Williams[1], Philip L. Croteau[1], Manuela Cirtog[3], Anaïs Féron[3], Jean-Eudes Petit[4], Alexandre Albinet[5], Jose L. Jimenez[6], and Zhe Peng[6]

[1]Center for Aerosol and Cloud Chemistry, Aerodyne Research Inc., Billerica, MA, USA
[2]Dept. of Chemistry, Drexel University, Philadelphia, PA, USA
[3]Laboratoire Inter-Universitaire des Systèmes Atmosphériques (LISA), UMR CNRS 7583, Université Paris-Est-Créteil, Université de Paris, Institut Pierre Simon Laplace (IPSL), Créteil, France
[4]Laboratoire des Sciences du Climat et de l'Environnement (CNRS-CEA-UVSQ), CEA Orme des Merisiers, Gif-sur-Yvette, France
[5]Institut National de l'Environnement Industriel et des Risques (Ineris), Verneuil-en-Halatte, France
[6]Dept. of Chemistry and Cooperative Institute for Research in Environmental Sciences (CIRES), University of Colorado, Boulder, CO, USA

Correspondence: Andrew T. Lambe (lambe@aerodyne.com), Zhe Peng (zhe.peng@colorado.edu)

Abstract. Oxidation flow reactors (OFRs) are an emerging tool for studying the formation and oxidative aging of organic aerosols and other applications. The majority of OFR studies to date involved generation of the hydroxyl radical (OH) to mimic daytime oxidative aging processes. On the other hand, use of the nitrate radical (NO_3) in modern OFRs to mimic nighttime oxidative aging processes has been limited due to the complexity of conventional techniques that are used to generate NO_3.

5　Here, we present a new method that uses a laminar flow reactor (LFR) to continuously generate dinitrogen pentoxide (N_2O_5) in the gas phase at room temperature from the $NO_2 + O_3$ and $NO_2 + NO_3$ reactions. The N_2O_5 is then injected into a dark Potential Aerosol Mass OFR and decomposes to generate NO_3; hereafter, this method is referred to as "OFR-iN_2O_5" ("i" = injected). To assess the applicability of the OFR-iN_2O_5 method towards different chemical systems, we present experimental and model characterization of the integrated NO_3 exposure, $NO_3:O_3$, $NO_2:NO_3$, and $NO_2:O_2$ as a function of LFR and OFR

10　conditions. These parameters were used to investigate the fate of representative organic peroxy radicals (RO_2) and aromatic alkyl radicals generated from volatile organic compound (VOC) + NO_3 reactions, and VOCs that are reactive towards both O_3 and NO_3. Finally, we demonstrate the OFR-iN_2O_5 method by generating and characterizing secondary organic aerosol from the β-pinene + NO_3 reaction.

1 Introduction

15　The importance of nitrate radicals (NO_3) as a nighttime oxidant is well established (Wayne et al., 1991; Brown and Stutz, 2012; Ng et al., 2017). In the atmosphere, $NO_2 + O_3$ is the primary source of NO_3, after which NO_3 exists in equilibrium with

NO_2 and N_2O_5. Atmospheric nighttime NO_3 mixing ratios can vary by at least two orders of magnitude, ranging from 1 ppt or less in remote areas to 10-400 ppt in polluted urban regions (Finlayson-Pitts and Pitts Jr., 2000; Asaf et al., 2010; Warneck and Williams, 2012; Ng et al., 2017). Atmospheric organic compounds that are reactive towards NO_3 include isoprene and monoterpenes that are emitted from biogenic sources (including urban vegetation); phenols and methoxyphenols emitted from

5   biomass burning; and polycyclic aromatic hydrocarbons (PAHs) emitted from combustion processes. NO_3 oxidation of these compounds generates oxygenated volatile organic compounds (OVOCs) and/or secondary organic aerosol (SOA), including particulate organic nitrates or nitroaromatics. The importance of these sources and processes are likely to continue to increase for the foreseeable future due to climate change (Melaas et al., 2016; Short, 2017).

    Laboratory studies have attempted to elucidate the mechanisms associated with NO_3-initiated oxidative aging processes, in

10 the gas and condensed phase, and in environmental chambers and flow tubes. Traditional NO_3 generation techniques typically utilize N_2O_5 as the radical precursor. N_2O_5 is generated from the reaction $NO + O_3 \rightarrow NO_2 + O_2$, followed by the reactions $NO_2 + O_3 \rightarrow NO_3 + O_2$ and $NO_2 + NO_3 \rightarrow N_2O_5$. The synthesized N_2O_5 is collected and stored in a cold trap under dry conditions to minimize hydrolysis of N_2O_5 to nitric acid (HNO_3). This method has limitations that hinder widespread usage: specifically, long-term storage and handling of N_2O_5 at low temperature and dry conditions is difficult, and continuous

15 generation of N_2O_5 as is required for oxidation flow reactors (OFRs) or other continuous flow chambers is challenging. Field studies investigating the NO_3-induced SOA formation potential of ambient air are thus extremely limited (Palm et al., 2017). Alternative NO_3 generation techniques that utilize reactions between chlorine atoms and chlorine nitrate ($ClONO_2$) or fluorine atoms and HNO_3 require cold storage of $ClONO_2$ and handling or generation of reactive halogen species that are reactive towards organic compounds (Burrows et al., 1985).

20 To address issues associated with traditional NO_3 generation techniques, we developed and characterized a new method that is well suited to applications where a continuous source of N_2O_5/NO_3 is required, such as OFR studies. The method is capable of continuous N_2O_5 generation in the gas phase at room temperature using a laminar flow reactor (LFR) that is coupled to a dark OFR in which N_2O_5 injected into the OFR decomposes to generate NO_3 and initiate oxidation of reactive VOCs. Hereafter, we refer to this method as "OFR-iN_2O_5" ("i" = injected"). We present experimental and model characterization

25 of OFR-iN_2O_5 as a function of LFR and OFR conditions, and we demonstrate application of OFR-iN_2O_5 to generate and characterize SOA from the β-pinene + NO_3 reaction.

2   Methods

2.1 N_2O_5 and NO_3 generation

Figure 1 shows a process flow diagram of the OFR-iN_2O_5 method. Separate flows containing NO_2 and O_3 were input to a PFA

30 tube with 2.54 cm outer diameter, 2.22 cm inner diameter, and 152.4 cm length that was operated as a LFR (Wood et al., 2003; Boyd et al., 2015). A compressed gas cylinder containing $1.00 \pm 0.02\%$ NO_2 in N_2 (Praxair) was used to supply NO_2. While not used for this study, replacing NO_2 with NO to avoid NO_2-to-HNO_3 conversion inside the gas cylinder and increasing [O_3] accordingly achieves similar results. O_3 was generated by passing 1750-1800 cm^3 min^{-1} of pure O_2 through a custom

Atmospheric
Measurement
Techniques
Discussions

Open Access

O$_3$ chamber housing a mercury fluorescent lamp (GPH212T5VH, Light Sources, Inc.) or 500-1800 cm^3 min^{-1} O$_2$ through a corona discharge ozone generator (Enaly 1KNT). We used 1800 cm^3 min^{-1} of O$_2$ carrier gas flow through the LFR (Re $\sim$ 110, i.e. laminar flow) to achieve τ_{LFR} = 20 s for reasons that are discussed in Section 3.1. The NO$_2$ mixing ratio entering the LFR, [NO$_2$]$_{0,LFR}$, was calculated from the NO$_2$ mixing ratio in the compressed gas mixture and the dilution ratio of 0-50

5   cm^3 min^{-1} or 0-1300 cm^3 min^{-1} gas flow into O$_2$ which was controlled using mass flow controllers. The O$_3$ mixing ratio entering the LFR, [O$_3$]$_{0,LFR}$, was measured using a 2B Technologies 106-MFT or a Teledyne M452 flow-through O$_3$ analyzer when generated from the mercury lamp or corona discharge source respectively. The output of the LFR was mixed with a carrier gas containing 3.8 L min^{-1} synthetic air and then injected into a Potential Aerosol Mass OFR (Aerodyne Research, Inc.), which is a horizontal 13.3 L aluminum cylindrical chamber operated in continuous flow mode (Kang et al., 2007; Lambe

10 et al., 2011, 2019) with 6.5 L min^{-1} flow through the reactor. The mean residence time in the OFR (τ_{OFR}) was 120 $\pm$ 34 s ($\pm$ 1σ), as obtained from measurements of 10 s pulsed inputs of NO$_2$ to the OFR obtained using a 2B Technologies Model 405 NO$_x$ analyzer (Figure S1). Across all experiments, the relative humidity in the OFR (RH$_{OFR}$) was controlled in the range of 7-85% at 23-25° C by passing the carrier gas through a Nafion humidifier (Perma Pure LLC) or heated recirculating water bath (Neslab Instruments, Inc.) prior to mixing with the LFR outflow. The O$_3$ mixing ratio at the exit of the OFR was measured

15 with a 2B Technologies Model 106-M ozone analyzer.

2.1.1   OFR-iN$_2$O$_5$ characterization studies

In one set of experiments, the integrated NO$_3$ exposure (NO$_{3exp}$), defined here as the product of the average NO$_3$ concentration and τ_{OFR}, was characterized by measuring the decay of VOC tracers reactive towards NO$_3$ using a Tofwerk/Aerodyne Vocus Proton Transfer Reaction Time-of-Flight Mass Spectrometer (PTR-MS) (Krechmer et al., 2018). For this purpose, the

20 tracer decay method is advantageous to direct NO$_3$ measurements at the OFR inlet and/or outlet because potential NO$_3$ concentration gradients inside the OFR that might otherwise bias NO$_{3exp}$ are easily accounted for. Tracers that were liquid at room temperature were injected into the OFR through a 10.2 cm length of 0.0152 cm ID Teflon tubing at a liquid flow rate of about 0.94 μL hr^{-1} using a syringe pump, prior to evaporation into a 2.4 L min^{-1} N$_2$ carrier gas. In preliminary studies, tracers such as isoprene and β-pinene were too reactive towards NO$_3$ to facilitate accurate characterization of NO$_{3exp}$ over the majority

25 of OFR-iN$_2$O$_5$ conditions that were investigated. Thus, experiments described in this paper used mixtures of tracers with bimolecular k_{NO_3} ranging from approximately 10^{-16} to 10^{-13} cm^3 molecules^{-1} s^{-1} and k_{O_3} < 10^{-19} cm^3 molecules^{-1} s^{-1} (Table S1). Acetonitrile was used as a nonreactive tracer. In "low O$_3$" experiments ([O$_3$]$_{0,LFR}$ = 10 to 300 ppm) a mixture of acetonitrile, butanal, thiophene, 2,3-dihydrobenzofuran, and naphthalene-d$_8$ (C$_{10}$D$_8$), each with mixing ratios of approximately 660 ppb, 50 ppb, 56 ppb, 40 ppb, and 18 ppb, respectively, was used. For this tracer mixture, the total external NO$_3$

30 reactivity (NO$_3$R$_{ext}$), which is the summed product of each tracer mixing ratio and its NO$_3$ rate constant, was approximately 0.07 s^{-1}. Naphthalene-d$_8$ was introduced by flowing 5 cm^3 min^{-1} N$_2$ through a Teflon tube packed with solid C$_{10}$D$_8$. In "high O$_3$" experiments ([O$_3$]$_{0,LFR}$ = 6100 to 7400 ppm), which generated higher NO$_{3exp}$, a mixture of acetonitrile (275 ppb), toluene (45 ppb), o-xylene (40 ppb), p-cymene (31 ppb), 1,2,4-trimethylbenzene (35 ppb), 1-butanol (53 ppb), benzaldehyde (47 ppb), butanal (53 ppb), and thiophene (56 ppb) was used, with NO$_3$R$_{ext}$ $\approx$ 0.38 s^{-1}.

In another set of experiments that were conducted as part of the Aerosol Chemical Monitor Calibration Center (ACMCC) particulate organonitrates (pON) experiment (Albinet et al., 2019), direct measurements of NO_3 generated via OFR-iN_2O_5 were performed using a newly developed Incoherent Broad Band Cavity Enhanced Absorption Spectroscopy (IBBCEAS) technique (Cirtog et al., manuscript in preparation). The IBBCEAS instrument that was used measured absorption as a function

5   of wavelength between λ = 640 and 680 nm, thereby allowing simultaneous measurements of NO_2 and and O_3 along with NO_3. During this experiment, pON were generated in a PAM OFR that used $[O_3]_{0,\mathrm{LFR}}$ = 150-180 ppm and $[NO_2]_{0,\mathrm{LFR}}$:$[O_3]_{0,\mathrm{LFR}}$ = 0.75, 1.0, and 2.0. IBBCEAS has been used to measure trace NO_3 levels in laboratory and field studies (Venables et al., 2006; Kennedy et al., 2011) using measurement principles that are described in detail by Romanini et al. (1997) and Langridge et al. (2008). Briefly, measurements were conducted by exciting a high-finesse optical cavity formed by two high reflectivity

10   mirrors with an incoherent broad-band-source centered on the λ = 662 nm absorption cross section of NO_3. Photons resonate between the two mirrors, allowing an effective path length of up to 4.5 km inside the cavity. The absorption coefficient of the sample in the cavity, $\alpha(\lambda)$, was calculated using Equation 1:

$$\alpha(\lambda) = \left(\frac{I_0(\lambda)}{I(\lambda)} - 1 \right) \left(\frac{1 - R(\lambda)}{d} \right) \tag{1}$$

Where $I(\lambda)$ and $I_0(\lambda)$ were the measured transmitted intensities in the presence and absence of NO_3, respectively, d = 61 cm

15   was the distance between the cavity mirrors, and $R(\lambda)$ was the mirror reflectivity ($\sim$99.98%), which was measured before each experiment using a certified calibration cylinder containing 600 ppb NO_2 in zero air (Air Liquide). NO_3 concentrations were calculated from the Beer-Lambert law using the measured α_{662} values and a NO_3 absorption cross section of 2×10^{-17} cm^2 at λ = 662 nm (Vandaele et al., 1998; Orphal et al., 2003). To avoid saturation of the IBBCEAS in these experiments, the OFR sample was diluted by a controlled dilution factor ranging from 9 to 50 and the detection response was deliberately lowered by

20   reducing the optical path length.

To demonstrate the application of OFR-iN_2O_5 to generate SOA, the chemical composition and mass concentration of β-pinene + NO_3 condensed-phase oxidation products was measured with an Aerodyne long-time-of-flight aerosol mass spectrometer (L-ToF-AMS) and/or an aerosol chemical speciation monitor (ACSM). A syringe pump was used to deliver β-pinene (10% (v/v) in carbon tetrachloride or 50% (v/v) in ethanol) into the carrier gas flow at liquid flow rates ranging from 0.94 to 19

25   μL hr^{-1}. Results presented in this paper assume an AMS/ACSM collection efficiency of 0.5 (Middlebrook et al., 2012) and a relative ionization efficiency of particulate organics equal to 1.6 (Xu et al., 2018).

2.2 Photochemical model

We used the KinSim chemical kinetic solver to calculate concentrations of radical/oxidant species (Peng et al., 2015; Peng and Jimenez, 2017, 2019). The KinSim mechanism shown in Table S2 was adapted from Palm et al. (2017) to model NO_3 and

30   N_2O_5 concentrations in the LFR and OFR. Inputs to the LFR-KinSim model were: $[O_3]_{0,\mathrm{LFR}}$, $[NO_2]_{0,\mathrm{LFR}}$, RH = 1%, T = 24°C, τ_{LFR} = 20 s (modeled as plug flow, see Section 3.1), and first-order wall loss rates of NO_3 and N_2O_5 (k_{wLFR,NO_3} and k_{wLFR,N_2O_5}). Inputs to the OFR-KinSim model were: $[O_3]$, $[NO_2]$, $[NO_3]$, and $[N_2O_5]$ output from the LFR and scaled by a

measured dilution factor of 4.4; RH and T measured in the OFR; τ_{OFR} = 120 s, $k_{\text{wOFR,NO}_3}$, and $k_{\text{wOFR,N}_2\text{O}_5}$, and input VOC tracer concentrations and their k_{NO_3} values. Because the calculated N_2O_5 residence time in the OFR inlet ($\sim$0.04 s) was short compared to the N_2O_5 decomposition timescale at T = 23 - 25 °C ($\sim$20 s), potential thermal decomposition of N_2O_5 during the dilution step was not considered in the model.

5 **2.2.1 LFR and OFR $k_{\text{w,NO}_3}$ and $k_{\text{w,N}_2\text{O}_5}$ values**

Published $k_{\text{w,NO}_3}$ values onto Teflon/Pyrex tubing with 1 cm and 4 cm ID are 0.2 and 0.1 s^{-1} respectively (Dubé et al., 2006; Wood et al., 2003), which bound the 2.22 cm ID of the LFR used in this study. Assuming k_w is inversely proportional to the internal diameter of the tube, we assumed $k_{\text{wLFR,NO}_3}$ = 0.15 s^{-1}. Extrapolating this value to the OFR yielded $k_{\text{wOFR,NO}_3}$ = 0.02 s^{-1}. At fixed OFR-iN$_2$O$_5$ conditions, varying $k_{\text{wLFR,NO}_3}$ between 0 and 0.2 s^{-1} changed $\text{NO}_{3\text{exp}}$ achieved in the OFR by

10 0.3%. Results were even less sensitive to $k_{\text{wOFR,NO}_3}$ assumed for the OFR because of its larger diameter and higher $\text{NO}_3\text{R}_{\text{ext}}$.
Published $k_{\text{w,N}_2\text{O}_5}$ values onto dry (RH $\approx$ 20%) Pyrex/PFA tubing with 4 and 7 cm ID are 0.04 and 0.009 s^{-1} respectively (Wagner et al., 2008; Gržinić et al., 2015). Extrapolating these values to the LFR used here yielded $k_{\text{w,N}_2\text{O}_5}$ values of 0.07 and 0.03 s^{-1} respectively. We therefore assumed $k_{\text{w,N}_2\text{O}_5}$ = 0.05 s^{-1} in the LFR-KinSim model. In preliminary OFR-KinSim modeling studies, we assumed $k_{\text{w,N}_2\text{O}_5}$ = 0.014 s^{-1} (Palm et al., 2017). However, as will be discussed in Section 3.3, $k_{\text{w,N}_2\text{O}_5}$

15 was humidity-dependent and required modifications to match measured $\text{NO}_{3\text{exp}}$ values as a function of RH_{OFR}.

3 Results and Discussion

3.1 LFR design considerations

The optimal LFR residence time (τ_{LFR}) was identified using model simulations of the injection of 300 ppm O$_3$ and NO$_2$ into the LFR followed by dilution and injection of the LFR output into an OFR operated with τ_{OFR} = 120 s. Figure S2 plots

20 $\text{NO}_{3\text{exp}}$ achieved in the OFR as a function of τ_{LFR} ranging from 1 to 60 s. Potential entry length effects that may have influenced results obtained below $\tau_{\text{LFR}} \approx$ 4-5 s were not considered in the model. Figure S2 shows that maximum $\text{NO}_{3\text{exp}}$ in the OFR was obtained at τ_{LFR} = 20 s at room temperature (unheated case); other $\text{NO}_{3\text{exp}}$ values were normalized to this condition. Below τ_{LFR} = 20 s, $\text{NO}_{3\text{exp}}$ was suppressed due to higher NO$_2$ levels entering the OFR. Above τ_{LFR} = 20 s, $\text{NO}_{3\text{exp}}$ was suppressed due to lower N$_2$O$_5$ levels entering the OFR because of more extensive LFR wall loss.

25 In traditional studies of NO$_3$ oxidative aging processes that are conducted at low pressure and short residence time ($\tau \sim$ 1 s), N$_2$O$_5$ is heated to generate a burst of NO$_3$ prior to injection into the system (Knopf et al., 2011). While not experimentally considered in this work, we modeled the $\text{NO}_{3\text{exp}}$ achieved assuming complete thermal dissociation of N$_2$O$_5$ between the LFR and OFR - for example, by heating to 120°C for 300 ms (Wood et al., 2003). Figure S2 suggests that the effect of heating N$_2$O$_5$ on $\text{NO}_{3\text{exp}}$ was most significant at short τ_{LFR}, where [N$_2$O$_5$] at the exit of the LFR was higher due to less wall loss

30 and room-temperature decomposition. For example, at τ_{LFR} = 8 s, the modeled $\text{NO}_{3\text{exp}}$ was 2.8 times higher in the complete-dissociation case than in the unheated case, whereas $\text{NO}_{3\text{exp}}$ increased by factors of 2.3 and 1.5 at τ_{LFR} = 20 and 60 s. Thus,

Atmospheric
Measurement
Techniques
Open Access
Discussions

EGU

a combination of reducing τ_{LFR} and heating N_2O_5 at the exit of the LFR increases $NO_{3\mathrm{exp}}$, and should be explored for future advanced implementations of OFR-iN_2O_5.

3.2   Example OFR-iN_2O_5 characterization studies

Figure 2a shows time series of O_3 and NO_2 concentrations during an OFR-iN_2O_5 characterization experiment where RH_{OFR}

5 = 11%, $[O_3]_{0,\mathrm{LFR}}$ = 280 ppm, and $[NO_2]_{0,\mathrm{LFR}}$ = 0 to 320 ppm. Figure 2b shows time series of acetonitrile (C_2H_3N), butanal (C_4H_8O), thiophene (C_4H_4S), 2,3-dihydrobenzofuran (C_8H_8O) and naphthalene-d$_8$ ($C_{10}D_8$) signals measured during the same period. Following NO_3 generation, the fractional decay of C_2H_3N, C_4H_8O, C_4H_4S and C_8H_8O increased with increasing tracer k_{NO_3} as expected. C_8H_8O was too reactive to measure any significant changes in its decay as a function of OFR-iN_2O_5 conditions shown in Figure 2; however, maximum decay of C_4H_8O and C_4H_4S was observed at $[NO_2]_{0,\mathrm{LFR}}:[O_3]_{0,\mathrm{LFR}}$

10 ≈ 0.7 in this experiment. Decay of naphthalene-d$_8$, which was influenced by both NO_3 and NO_2 concentrations (Table S1), was maximized at $[NO_2]_{0,\mathrm{LFR}}:[O_3]_{0,\mathrm{LFR}}$ ≈ 0.3 to 1.1.

To confirm that VOC degradation shown in Fig. 2b was due to reaction with NO_3, Figure 3 shows IBBCEAS measurements of NO_3 obtained in separate OFR-iN_2O_5 characterization experiments that used $[O_3]_{0,\mathrm{LFR}}$ = 150-160 ppm and $[NO_2]_{0,\mathrm{LFR}}:[O_3]_{0,\mathrm{LFR}}$ = 0.75 and 2.0. The maximum IBBCEAS signal observed at λ = 662 nm indicated the presence of

15 NO_3, as is evident from comparison with the wavelength-dependent absorption cross section of NO_3 obtained by Orphal et al. (2003) and plotted in Figure 3b. Additionally, Figure S3 shows the relative rate coefficient obtained from the decay of C_4H_8O and C_4H_4S measured with PTR-MS. We measured a relative rate coefficient of 2.83, which is in agreement with a relative rate coefficent value of 3.22 $\pm$ 0.95 calculated from $C_4H_8O + NO_3$ and $C_4H_4S + NO_3$ rate coefficients (Atkinson, 1991; D'Anna et al., 2001). Ions corresponding to peroxy butyl nitrate, nitrothiophene, and nitronaphthalene-d$_7$, which are known NO_3 oxi-

20 dation products of C_4H_8O, C_4H_4S, and $C_{10}D_8$, respectively (Atkinson et al., 1990; Jenkin et al., 2003; Saunders et al., 2003; Cabañas et al., 2005), were also detected with PTR-MS. Tracer decay experiments similar to the measurements shown in Figure 2 were repeated over $[O_3]_{0,\mathrm{LFR}}$ ranging from 10 to 7400 ppm, $[NO_2]_{0,\mathrm{LFR}}$ ranging from 0 to 7200 ppm, and RH_{OFR} ranging from 7 to 85%. For experiments where $[O_3]_{0,\mathrm{LFR}}$ > 6000 ppm, $NO_{3\mathrm{exp}}$ was calculated from the decay of o-xylene because (1) p-cymene has a large ionized fragment at $C_7H_9^+$ (thus interfering with detection of toluene that was also present), (2) NO_3

25 oxidation products were generated that interfered with detection of oxygenated tracers (butanol, benzaldehyde, butanal) and(3) the remaining tracers that were used were too reactive towards NO_3 to accurately constrain $NO_{3\mathrm{exp}}$.

3.3   Effect of RH_{OFR}, $[O_3]_{0,\mathrm{LFR}}$, and $[NO_2]_{0,\mathrm{LFR}}$ on $NO_{3\mathrm{exp}}$

Figure 4 shows $NO_{3\mathrm{exp}}$ as a function of RH_{OFR} at $[O_3]_{0,\mathrm{LFR}}$ = 250 ppm and $[NO_2]_{0,\mathrm{LFR}}$ = 130 ppm. At these conditions, $NO_{3\mathrm{exp}}$ decreased from 1.2×10^{14} to 2.0×10^{13} molecules cm^{-3} s as RH_{OFR} increased from 11% to 81%. We hypothesize

30 that this result is due to more efficient hydrolysis of N_2O_5 to HNO_3 on the wetted walls of the OFR at higher RH, thereby suppressing $NO_{3\mathrm{exp}}$ relative to values obtained at lower RH conditions. In an attempt to model this behavior, k_{w,N_2O_5} values input to the model were adjusted as a function of RH_{OFR}. Figure 4 suggests that humidity-dependent k_{w,N_2O_5} values ranging from 0.01 to 0.08 s^{-1} were required to cover the range of measured $NO_{3\mathrm{exp}}$. These values agreed within a factor of 2 or better

with humidity-dependent k_{w,N_2O_5} values ranging from 0.014 to 0.040 s^{-1} measured by Palm et al. (2017) in a similar OFR and were applied in subsequent model calculations.

Figure 5 shows NO_{3exp} as a function of $[O_3]_{0,LFR}$ for measurements with $[NO_2]_{0,LFR}:[O_3]_{0,LFR} = 0.5 \pm 0.1$ and RH_{OFR} = 11 ± 2%. The equivalent ambient photochemical age shown on the right y-axis was calculated assuming a 14-hour average

5   nighttime NO_3 mixing ratio of 30 ppt and a 10-hour daytime NO_3 mixing ratio of 0 ppt (Asaf et al., 2010). NO_{3exp} increased with increasing $[O_3]_{0,LFR}$ due to increased NO_3 production from higher $[N_2O_5]$. Over the range of measured conditions, increasing $[O_3]_{0,LFR}$ from 33 to 7092 ppm increased NO_{3exp} from 6.4×10^{12} to 4.0×10^{15} molec cm^{-3} s^{-1}. The black line in Figure 5 represents NO_{3exp} modeled using the mechanism shown in Table S2. Measured and modeled NO_{3exp} values agreed within a factor of 2 or better above $[O_3]_{0,LFR} \approx 40$ ppm, and the gain in NO_{3exp} as a function of $[O_3]_{0,LFR}$ was highest

10   between $[O_3]_{0,LFR} \approx 10$ and 300 ppm. Over this range of $[O_3]_{0,LFR}$, the NO_2 oxidation lifetime with respect to O_3 decreased from 115 s to 4 s. Because τ_{LFR} = 20 s, in this range of LFR conditions, the NO_2 lifetime in the LFR was long enough that high NO_2 levels exiting the LFR suppressed NO_{3exp} in the OFR. On the other hand, increasing $[O_3]_{0,LFR}$ from 300 to 7000 ppm decreased the NO_2 oxidation lifetime with respect to O_3 from 4 s to 0.2 s, and $[NO_2]$ exiting the LFR was too low to significantly affect NO_{3exp}. To support this hypothesis, Figure 6 plots NO_{3exp} as a function of $[NO_2]_{0,LFR}:[O_3]_{0,LFR}$ at

15   $[O_3]_{0,LFR} = 250 \pm 20$ ppm and 6850 ± 400 ppm. Here, we incorporated NO_{3exp} values obtained over RH_{OFR}= 11% to 81% for better statistics, and normalized each NO_{3exp} value to the maximum NO_{3exp} obtained at the same RH. Figure 6 shows that at $[O_3]_{0,LFR}$= 250 ppm, maximum $NO_{3,exp}$ was achieved at $[NO_2]_{0,LFR}:[O_3]_{0,LFR} \approx 0.5$ to 0.7. On the other hand, at $[O_3]_{0,LFR} = 6850$ ppm, maximum NO_{3exp} value was achieved at $[NO_2]_{0,LFR}:[O_3]_{0,LFR} \approx 1.2$.

In a related set of experiments, IBBCEAS measurements of the $NO_2:NO_3$ ratio at the exit of the OFR (obtained from

20   Figure 3a spectra) confirmed that significantly higher NO_2 levels were present in the OFR at higher $[NO_2]_{0,LFR}:[O_3]_{0,LFR}$, as expected. For example, at $[O_3]_{0,LFR} = 150$ ppm and $[NO_2]_{0,LFR} = 112$ ppm, $NO_2:NO_3 = 28$, whereas at $[O_3]_{0,LFR} = 160$ ppm and $[NO_2]_{0,LFR} = 320$ ppm, $NO_2:NO_3 = 613$. $NO_2:NO_3$, along with $NO_3:O_3$ and $NO_2:NO_3$, has important implications for the fate of organic species in OFR-iN_2O_5 that are discussed in the following sections.

3.4   Model characterization of OFR-iN_2O_5: $NO_3:O_3$, $NO_2:NO_3$, and $NO_2:O_2$

25   To examine OFR-iN_2O_5 performance over a wider range of conditions, Figure 7 plots the mean NO_{3exp}, $[O_3]$, $NO_3:O_3$, $NO_2:NO_3$, and $NO_2:O_2$ values obtained with the model as a function of $[O_3]_{0,LFR} = 10$ ppm to 10^5 ppm (10%), for $[NO_2]_{0,LFR}:[O_3]_{0,LFR} = 0.01, 0.1, 0.5, 1.0, 1.5, 1.8$ and 2.0. Three observations are apparent from Figure 7. First, at $[O_3]_{0,LFR}$ < 1000 ppm and $[NO_2]_{0,LFR}:[O_3]_{0,LFR} = 0.1$ to 1.8, maximum NO_{3exp} increased with decreasing $[NO_2]_{0,LFR}:[O_3]_{0,LFR}$ (Fig. 7a). Above $[O_3]_{0,LFR} \approx 2000$ ppm, NO_{3exp} was less sensitive to $[NO_2]_{0,LFR}:[O_3]_{0,LFR}$. Second, maximum $NO_3:O_3$ in-

30   creased with increasing $[NO_2]_{0,LFR}:[O_3]_{0,LFR}$ (Figure 7c). Third, the $[NO_2]_{0,LFR}:[O_3]_{0,LFR} = 2.0$ case demonstrated unique behavior relative to the other cases because residual O_3 exiting the LFR was low (< 10 ppm) because of nearly complete conversion of O_3 to N_2O_5 inside the LFR (Figure 7b). Consequently, the high residual $[NO_2]$ suppressed NO_{3exp} by one to two orders of magnitude relative to $[NO_2]_{0,LFR}:[O_3]_{0,LFR} < 2$ cases (Fig. 7a) and generated enhanced $NO_3:O_3$, $NO_2:NO_3$, and $NO_2:O_2$ values. In addition, $NO_2:NO_3$ ratios obtained from IBBCEAS measurements at $[O_3]_{0,LFR} = 150$ to 160 ppm

and $[NO_2]_{0,LFR}$:$[O_3]_{0,LFR}$ = 0.75, 1.0 and 2.0 are shown in Figure 7d. The measured NO_2:NO_3 values are comparable to, or lower than, the modeled NO_2:NO_3 values obtained at similar conditions, and therefore broadly support using model results to further investigate the fate of (1) RO_2 that are formed from NO_3 oxidation of VOCs, (2) alkyl radicals that are reactive towards NO_2 and O_2, and (3) VOCs that are reactive towards O_3 and NO_3 in the following sections.

3.4.1 Fate of organic peroxy radicals (RO_2) formed from NO_3 + VOC reactions

RO_2 react with NO, NO_2, NO_3, HO_2, or other RO_2 to generate alkoxy (RO) radicals, peroxynitrates (RO_2NO_2), hydroperoxides or organic peroxides, and may additionally undergo autooxidation via sequential isomerization and O_2 addition. To investigate the fate of RO_2 as a function of OFR-iN_2O_5 conditions, we applied the methodology of Peng et al. (2019) by calculating the fractional oxidative loss of a generic alkyl or acyl RO_2 to each of these species over the range of conditions shown in Figure 7. Kinetic data from Orlando and Tyndall (2012) that was used in these calculations is summarized in Table S3. Under almost all OFR-iN_2O_5 conditions shown in Figure 7, RO_2 reactions with NO, HO_2, and RO_2 were minor ($< 1\%$) loss pathways compared to reaction with NO_2 and NO_3, although the RO_2 + RO_2 pathway is potentially more important at higher NO_3R_{ext}. To investigate the relative importance of competing RO_2 + NO_2 and RO_2 + NO_3 pathways, we defined the fractional reactive loss of RO_2 due to NO_3, $F_{RO_2+NO_3}$:

$$F_{RO_2+NO_3} = \frac{k_{NO_3}[NO_3]}{k_{NO_3}[NO_3] + k_{NO_2}[NO_2]} \tag{2}$$

Figures 8a and 8b show $F_{RO_2+NO_3}$ calculated for alkyl and acyl RO_2 respectively. To simplify the analysis, we assumed that the thermal decomposition of RO_2NO_2 species formed from RO_2 + NO_2 reactions was slow compared to τ_{OFR}. This assumption generates a lower limit $F_{RO_2+NO_3}$ value for the alkyl RO_2 case, where RO_2NO_2 decomposition occurs on timescales of seconds or less (Orlando and Tyndall, 2012)), but has minimal influence on the acyl-RO_2 case due to higher thermal stability of peroxyl acyl nitrates. For alkyl RO_2, Figure 8a shows that $F_{RO_2+NO_3}$ = 0.5 was achieved between $[NO_2, O_3]_{0,LFR}$ = (125 ppm, 250 ppm) and (3240 ppm, 1800 ppm). For acyl RO_2, due to faster reaction with NO_2, Figure 8b shows that $F_{RO_2+NO_3}$ = 0.5 was achieved using $[NO_2, O_3]_{0,LFR}$ = (350 ppm, 700 ppm) to (1.1%, 0.6%).

To investigate the feasibility of generating OFR-iN_2O_5 conditions where RO_2 loss is dominated by autooxidation, we calculated the lifetime of alkyl and acyl RO_2 (τ_{RO_2}) over the range of OFR-iN_2O_5 conditions shown in Figures 7 and 8a-b. As shown in Figures 8d-e, maximum $\tau_{RO_2} \approx 1.4$ s (alkyl) and 0.4 s (acyl) were obtained at $[NO_2]_{0,LFR} \approx 2$ ppm and $[O_3]_{0,LFR} \approx$ 200 ppm. At lower $[O_3]_{0,LFR}$, τ_{RO_2} decreased due to faster RO_2 + NO_2 reaction rate, and at higher $[O_3]_{0,LFR}$, τ_{RO_2} decreased due to faster RO_2 + NO_3 reaction rate. Because RO_2 autooxidation timescales range from 0.005 to 200 s depending on the specific RO_2 composition (Crounse et al., 2013), OFR-iN_2O_5 may achieve autooxidation-dominant conditions for some RO_2 but not for others.

3.4.2 Fate of aromatic alkyl radicals (R) formed from NO_3 + VOC reactions

The majority of R that are generated from NO_3 oxidation of VOCs quickly react with O_2 to generate RO_2. However, NO_3 oxidation of a subset of aromatic VOCs generates R that react more slowly with O_2, thereby enabling competing reactions

Atmospheric
Measurement
Techniques
Discussions

Open Access

EGU

with NO_2. For example, the phenoxy radical (C_6H_5O) generated from NO_3 oxidation of phenol (C_6H_5OH) has $k_{O_2}:k_{NO_2} < 2.4\times10^{-9}$ (Platz et al., 1998), and the $C_{10}H_7NO_3$ radical that is generated from NO_3 oxidation of naphthalene ($C_{10}H_8$) has $k_{O_2}:k_{NO_2} < 4\times10^{-7}$ (Atkinson et al., 1994). Alkyl radicals generated from NO_3 oxidation of other PAH may behave similarly to $C_{10}H_7NO_3$ but kinetic data are unavailable in the literature. To investigate the relative importance of competing $R + NO_2$ and $R + O_2$ reactions in these systems, we defined the fractional reactive loss of R with respect to O_2, F_{R+O_2}:

$$F_{R+O_2} = \frac{k_{O_2}[O_2]}{k_{O_2}[O_2] + k_{NO_2}[NO_2]} \tag{3}$$

Figure 8c shows F_{R+O_2} over the same OFR-iN_2O_5 operating conditions used to generate Figures 7 and 8a-b. For C_6H_5O (not shown), $F_{R+O_2} < 0.08$ over the entire range of OFR-iN_2O_5 conditions shown in Figures 7e and 8c. For $C_{10}H_7NO_3$, $F_{R+O_2} \geq 0.5$ was achieved for the majority of OFR-iN_2O_5 conditions where $[NO_2]_{0,LFR}:[O_3]_{0,LFR} \leq 0.1$, and also between $[NO_2, O_3]_{0,LFR} = (100\ ppm, 200\ ppm)$ and $(5000\ ppm, 10000\ ppm)$. The use of $[NO_2]_{0,LFR}:[O_3]_{0,LFR} \geq 1$ always generated conditions where the reaction rate of $R + NO_2$ exceeded $R + O_2$.

3.4.3 Fate of VOCs reactive towards O_3 and NO_3

We defined the fractional reactive loss of a VOC with respect to NO_3, F_{VOC+NO_3}:

$$F_{VOC+NO_3} = \frac{k_{NO_3}[NO_3]}{k_{NO_3}[NO_3] + k_{O_3}[O_3]} \tag{4}$$

and established $F_{VOC+NO_3} = 0.9$ as the criterion for NO_3-dominated oxidative loss. Figure 9 plots $NO_3:O_3$ at which F_{VOC+NO_3} = 0.9 for several classes of organic compounds with published k_{NO_3} and k_{O_3} values greater than 10^{-16} and 10^{-19} cm^{-3} molecules^{-1} s^{-1}, respectively. This figure therefore excludes compounds such as alkanes and monocyclic aromatics that react slowly with NO_3 and are essentially unreactive towards O_3 ($F_{NO_3} \approx 1$). $NO_3:O_3$ values that correspond to $[NO_2]_{0,LFR}$ and $[O_3]_{0,LFR} = [2\ ppm, 200\ ppm]$, $[150\ ppm, 300\ ppm]$, and $[5400\ ppm, 3000\ ppm]$ are represented by horizontal bands with upper and lower limit values calculated assuming k_{w,N_2O_5} values of 0.01 and 0.08 s^{-1} (Section 3.3). These LFR inputs generated OFR-iN_2O_5 conditions that maximize RO_2 lifetime and $NO_3:O_3$ at $[NO_2]:[O_3]_{0,LFR} = 0.5$ and 1.8, respectively (Figures 7-8). Figures 7 and 9 together with kinetic data in the literature suggest that injection of 2 ppm NO_2 and 200 ppm O_3 into the LFR was sufficient to achieve $F_{VOC+NO_3} \geq 0.9$ for phenols, PAHs with no double bonds, and mono- and sesquiterpenes with 1 double bond at low RH_{OFR}. Increasing $[NO_2]_{0,LFR}$ to 150 ppm and $[O_3]_{0,LFR}$ to 300 ppm additionally achieved $F_{VOC+NO_3} \geq 0.9$ for acenaphthylene, isoprene, and mono- and sesquiterpenes with 1 double bond at elevated RH_{OFR}. Further increasing $[NO_2]_{0,LFR}$ to 5400 ppm and $[O_3]_{0,LFR}$ to 3000 ppm achieved $F_{VOC+NO_3} \geq 0.9$ for $\geq$ C3 linear alkenes, unsaturated aldehydes, and mono- and sesquiterpenes with 2 double bonds at low RH_{OFR}. While $[NO_2,O_3] = [20\%, 10\%]$ (not shown) achieved $F_{VOC+NO_3} \geq 0.9$ for (E)-3-penten-2-one and ethene, the corresponding $NO_{3exp} \approx 10^{14}$ molecules cm^{-3} s achieved at this condition (Figure 7a) was insufficient to oxidize more than 1-2% of the initial ethene concentration due to its slow NO_3 rate constant (Atkinson, 1991).

3.5   NO₃ estimation equation for OFR-iN₂O₅

Previous studies reported empirical OH exposure algebraic estimation equations for use with OFRs (Li et al., 2015; Peng et al., 2015, 2018; Lambe et al., 2019). These equations parameterize OH_{exp} as a function of readily-measured experimental parameters, therefore providing a simpler alternative than detailed photohemical models for experimental planning and analysis. Here,

5   we expand on those studies by deriving an NO_{3exp} estimation equations for OFR-iN₂O₅. Model results obtained from the base case of the model – a VOC reacting with NO_3 at 2.5×10^{-12} cm³ molecule⁻¹ s⁻¹ as surrogate of NO_3R_{ext} – were used to derive the following equation that allows estimating NO_{3exp} for OFR-iN₂O₅:

$$\log[(NO_3)_{exp}] = a + b\log[273.15 + T_{OFR}] + c\log[\tau_{OFR}] + d\log[NO_2]_{0,LFR} + e\log[O_3]_{0,LFR} \cdot T_{OFR} \tag{5}$$

$$+ f\log[k_{w_{OFR},N_2O_5}] + \log\left(\frac{[NO_2]_{0,LFR}}{[O_3]_{0,LFR}}\right) \cdot (g\,(\log[O_3]_{0,LFR})^2 + h\log[O_3]_{0,LFR}) - \frac{[NO_2]_{0,LFR}}{[O_3]_{0,LFR}} \cdot (i + j\log[O_3]_{0,LFR})$$

10   $$+ k\log(NO_3R)_{ext} + l\log[NO_2]_{0,LFR} \cdot T + m\log[O_3]_{0,LFR} \cdot \log k_{w_{OFR},N_2O_5}$$

The phase space of OFR-iN₂O₅ parameters for fitting Equation 5 to NO_{3exp} model results was defined as follows: $[O_3]_{0,LFR}$ = 10-1000 ppm, $[NO_2]_{0,LFR}$ = 10-1000 ppm, $[NO_2]_{0,LFR}:[O_3]_{0,LFR} \leq 2$, NO_3R_{ext} = 1-200 s⁻¹, k_{w_{OFR},N_2O_5} = 0.01-0.08 s⁻¹, T_{OFR} = 0 - 40°C, and τ_{OFR} = 60 - 300 s. The cases where $O_3]_{0,LFR}$ > 1000 ppm and/or $[NO_2]_{0,LFR}:[O_3]_{0,LFR}$ > 2 were not considered because of less practical interest. We explored 11, 11, 7, 4, and 5 logarithmically evenly distributed values

15   in the ranges of $[O_3]_{0,LFR}$, $[NO_2]_{0,LFR}$ (11 values over 10–1000 ppm), NO_3R_{ext}, k_{w,N_2O_5}, and τ_{OFR}, respectively. Due to significantly different chemical regimes in different parts of the phase space, fit coefficients that are reported in Table 1 were obtained by fitting the same functional form (Equation 5) over 3 sub-phase spaces with the following additional constraints: (i) $[NO_2]_{0,LFR}:[O_3]_{0,LFR}$ = 0-1 and NO_3R_{ext} = 20-200 s⁻¹; (ii) $[NO_2]_{0,LFR}:[O_3]_{0,LFR}$= 0-1 and NO_3R_{ext} = 1-20 s⁻¹ (iii) $[NO_2]_{0,LFR}:[O_3]_{0,LFR}$ = 1-2. For these 3 subspaces, 10080, 13440, and 5880 model cases respectively were simulated. In

20   Equation 5, the terms involving the coefficients g–j were included to reproduce the relationship between normalized NO_{3exp} and $[NO_2]_{0,LFR}:[O_3]_{0,LFR}$ shown in Figure 5. Logarithms of first- and second-order terms were successively added until no further fit quality improvement was achieved. Figure 10 compares NO_{3exp} estimated from Equation 5 and calculated from the model described in Section 2.2. The mean absolute value of the relative deviation was 49% which is comparable with results obtained for previous estimation equations with significant NO_y chemistry (Peng et al., 2018).

25   ## 3.6   SOA generation from β-pinene + NO₃

To apply the OFR-iN₂O₅ technique to SOA formation studies, we generated SOA from β-pinene + NO_3 in the absence of seed particles using $[O_3]_{0,LFR}$ = 300 ppm, $[NO_2]_{0,LFR}$ = 150 ppm, and $RH_{OFR} \approx 1\%$. PTR-MS measurements confirmed complete consumption of β-pinene, and numerous product ions were detected. The largest ions detected were $(H^+)C_9H_{14}O$ and $(H^+)C_{10}H_{14}$ which may correspond to nopinone ($C_9H_{14}O$) and fragmentation/decomposition products of $C_{10}H_{17}NO_4$

30   respectively (Hallquist et al., 1999; Claflin and Ziemann, 2018). The mass yield of SOA ranged from 0.03 to 0.39 over β-pinene mixing ratios ranging from 20-400 ppbv that were injected into the OFR. These yield values are broadly consistent

with previous environmental chamber studies (Ng et al., 2017) but are lower than chamber SOA yields obtained at the same β-pinene mixing ratio, presumably due to the absence of seed particles in the OFR (Lambe et al., 2015). To compare results obtained using OFR-iN$_2$O$_5$ with a conventional environmental chamber method, Figures 11a-b show HR-ToF-AMS spectra of SOA generated from NO$_3$ oxidation of β-pinene in the Georgia Tech chamber (Boyd et al., 2015) and in the OFR, along with a

5   scatter plot of relative ion abundances present in the two spectra (Figure 11c). The same spectra are presented on a logarithmic scale in Figure S4. As is evident, β-pinene + NO$_3$ SOA generated in the chamber and OFR exhibit a high degree of similarity (linear regression slope = 0.98 and r^2 = 0.99). The largest ion signal was observed at NO$^+$, which, along with signal at NO$_2^+$ and NO$^+$: NO$_2^+$ = 6.7, is consistent with the formation of particulate organic nitrates (Farmer et al., 2010). Signals observed at CHO$^+$, C$_2$H$_3$O$^+$, and other C$_x$H$_y$O$_{>1}^+$ ions suggest the presence of other multifunctional oxidation products.

10   **4   Conclusions**

OFR-iN$_2$O$_5$ complements recently developed methods that enable NO$_x$-dependent photooxidation studies in OFRs such as OFR-iN$_2$O and OFR-iC$_3$H$_7$ONO (Lambe et al., 2017; Peng et al., 2018; Lambe et al., 2019) by enabling studies of nighttime NO$_3$-initiated oxidative aging processes. Important OFR-iN$_2$O$_5$ parameters are [O$_3$], [NO$_2$], [H$_2$O], T, NO$_3$R$_{ext}$, and τ_{OFR}. By contrast, important OFR-iN$_2$O and OFR-iC$_3$H$_7$ONO parameters are UV intensity, external OH reactivity (OHR$_{ext}$), τ_{OFR},

15   and either [O$_3$] + [H$_2$O] + [N$_2$O] or [C$_3$H$_7$ONO]. Notably, NO$_3$R$_{ext}$ is typically less significant in OFR-iN$_2$O$_5$ than OHR$_{ext}$ in OFR-iN$_2$O or OFR-iC$_3$H$_7$ONO because (1) most compounds are less reactive towards NO$_3$ than OH, (2) NO$_{3exp}$ is higher than OH$_{exp}$, and (3) the internal NO$_3$ reactivity of OFR-iN$_2$O$_5$, which is dominated by the NO$_3$ + NO$_2$ reaction, is larger and easier to manipulate than the internal OH reactivity of OFR-iN$_2$O and OFR-iC$_3$H$_7$ONO, which is dominated by OH + HO$_2$ and OH + NO$_2$ reactions. To identify optimal OFR-iN$_2$O$_5$ conditions for different applications, we characterized NO$_{3exp}$,

20   τ_{RO_2}, $F_{RO_2+NO_3}$, F_{R+O_2} and F_{VOC+NO_3} at [O$_3$]$_{0,LFR}$ = 10 ppm to 10%, [NO$_2$]$_{0,LFR}$:[O$_3$]$_{0,LFR}$ = 0.01 to 2.0, and RH$_{OFR}$ = 7 to 85%. Optimal NO$_{3exp}$ was achieved by minimizing [H$_2$O] in the OFR and associated humidity-dependent N$_2$O$_5$ wall losses. This is contrary to most OFR techniques that are used to generate OH radicals, where optimal OH$_{exp}$ is achieved by maximizing [H$_2$O] and associated OH production from the O(^{1}D) + H$_2$O reaction and/or H$_2$O photolysis at λ = 185 nm.

Figure 12 presents image plots that represent OFR-iN$_2$O$_5$ conditions suitable for generating optimal NO$_{3exp}$, NO$_3$:O$_3$,

25   NO$_2$:NO$_3$, and τ_{RO_2} values at the lower and upper-limit k_{w,N_2O_5} values that were measured. Most OFR-iN$_2$O$_5$ conditions using [O$_3$]$_{0,LFR}$ > 200 ppm generated NO$_{3exp}$ > 1.5×10^{12} molecules cm^{-3} s (Figures 12a-b), which is sufficient to oxidize isoprene and compounds with similar k_{NO_3}; for reference, NO$_{3exp}$ > 1.6×10^{11} molecules cm^{-3} s is required to oxidize α-pinene. At [O$_3$]$_{0,LFR}$ >200 ppm and [NO$_2$]$_{0,LFR}$:[O$_3$]$_{0,LFR}$ > 0.5, OFR-iN$_2$O$_5$ generated NO$_3$:O$_3$ > 10^{-3} at k_{w,N_2O_5} = 0.01 s^{-1} (Figure 12c), which achieved F_{VOC+NO_3} > 0.9 for mono- and sesquiterpenes with 1 double bond, most PAHs,

30   and phenol/methoxyphenol species. Achieving NO$_3$:O$_3$ > 10^{-3} at k_{w,N_2O_5} = 0.08 s^{-1} was more challenging (Figure 12d). Increasing [O$_3$]$_{0,LFR}$ decreased [NO$_2$]:[NO$_3$] and therefore increased $F_{RO_2+NO_3}$ (Figures 12e-f). On the other hand, decreasing [O$_3$]$_{0,LFR}$ or increasing k_{w,N_2O_5}, and, consequently, NO$_{3exp}$, increased τ_{RO_2} (Figures 12g-h), potentially allowing more time for autooxidation processes to occur. The best overlap between OFR-iN$_2$O$_5$ conditions that achieved $F_{RO_2+NO_3}$ > 0.9

and $\tau_{RO_2} > 1$ s were obtained with $[NO_2]_{0,LFR} \approx$ 2-3 ppm and $[O_3]_{0,LFR} \approx$ 200-300 ppm. Because atmospheric $NO_2:NO_3$ is highly variable and often much larger than $NO_2:NO_3$ achieved using OFR-iN_2O_5 (Brown et al., 2003; Stutz et al., 2004), simply attempting to maximize $F_{RO_2+NO_3}$ may not always be necessary and has tradeoffs such as decreasing $NO_3:O_3$ and F_{VOC+NO_3}. OFR-iN_2O_5 was more difficult to apply to species such as unsaturated carbonyls and mono- and sequiterpenes

5   with multiple double bonds that react more efficiently with O_3 than other VOCs; here, alternative NO_3 generation techniques that do not introduce O_3 to the OFR warrant consideration, even though they are more difficult to implement (Palm et al., 2017).

Because OFR-iN_2O_5 can continuously generate N_2O_5 and NO_3 at room temperature, it is significantly easier to apply in continuous flow reactor studies than related techniques. However, in addition to the aforementioned considerations, high N_2O_5

10   and HNO_3 concentrations that are generated using OFR-iN_2O_5 complicate the application of techniques such as iodide-adduct chemical ionization mass spectrometry due to efficient reactions between the iodide reagent ion and N_2O_5 or HNO_3 (Lee et al., 2014). Future applications of OFR-iN_2O_5 will investigate the NO_3-initiated OVOC and SOA formation potential of simple and complex precursors in laboratory and field studies.

Code and data availability. Data and KinSim mechanisms presented in this manuscript are available upon request. The KinSim kinetic

15   solver is freely available at http://tinyurl.com/kinsim-release.

Author contributions. AL, EW, and AA conceived and planned the experiments. AL, JK, FM, LW, PC, AA, and JEP carried out the experiments. MC and AF performed the IBBCEAS measurements and data analysis. AL, JJ and ZP conceived and planned the model simulations, and AL and ZP carried out the model simulations. AL, EW, ZP, and JJ contributed to the interpretation of the results. AL took the lead in writing the manuscript. All authors provided feedback on the manuscript.

20   *Competing interests.* The authors declare no competing interests.

References

Albinet, A., Petit, J.-E., Lambe, A. T., Kalogridis, A., Heikkinen, L., Graeffe, F., Cirtog, M., Féron, A., Allan, J. D., Bibi, Z., Amodeo, T., Karoski, N., Aujay-Plouzeau, R., Meunier, L., Gros, V., Bonnaire, N., Sarda-Estève, R., Truong, F., Ehn, M., Jokinen, T., Aurela, M., Maasikmets, M., Marin, C., Marmureanu, L., Eriksson, A., Ahlberg, E., Freney, E., Minguillon, M., Croteau, P. L., Jayne, J. T., Williams, L. R., and Favez, O.: Overview of the ACMCC particulate organonitrates (pON) experiment., in: 37th AAAR Conference, Portland, OR, USA, 2019.

Asaf, D., Tas, E., Pedersen, D., Peleg, M., and Luria, M.: Long-Term Measurements of NO_3 Radical at a Semiarid Urban Site: 2. Seasonal Trends and Loss Mechanisms, Environ. Sci. Technol., 44, 5901–5907, https://doi.org/10.1021/es100967z, 2010.

Atkinson, R.: Kinetics and Mechanisms of the Gas-Phase Reactions of the NO_3 Radical with Organic Compounds, Journal of Physical and Chemical Reference Data, 20, 459–507, https://doi.org/http://dx.doi.org/10.1063/1.555887, 1991.

Atkinson, R., Arey, J., Zielinska, B., and Aschmann, S. M.: Kinetics and nitro-products of the gas-phase OH and NO_3 radical-initiated reactions of naphthalene-d8, fluoranthene-d10, and pyrene, International Journal of Chemical Kinetics, 22, 999–1014, https://doi.org/10.1002/kin.550220910, 1990.

Atkinson, R., Tuazon, E. C., Bridier, I., and Arey, J.: Reactions of NO_3-naphthalene adducts with O_2 and NO_2, Int. J. Chem. Kinet., 26, 605–614, https://doi.org/10.1002/kin.550260603, 1994.

Boyd, C. M., Sanchez, J., Xu, L., Eugene, A. J., Nah, T., Tuet, W. Y., Guzman, M. I., and Ng, N. L.: Secondary organic aerosol formation from the β-pinene+NO_3 system: effect of humidity and peroxy radical fate, Atmospheric Chemistry and Physics, 15, 7497–7522, 2015.

Brown, S. S. and Stutz, J.: Nighttime radical observations and chemistry, Chem. Soc. Rev., 41, 6405–6447, https://doi.org/10.1039/C2CS35181A, 2012.

Brown, S. S., Stark, H., Ryerson, T. B., Williams, E. J., Nicks Jr., D. K., Trainer, M., Fehsenfeld, F. C., and Ravishankara, A. R.: Nitrogen oxides in the nocturnal boundary layer: Simultaneous in situ measurements of NO_3, N_2O_5, NO_2, NO, and O_3, J. Geophys. Res., 108, https://doi.org/10.1029/2002jd002917, 2003.

Burrows, J. P., Tyndall, G. S., and Moortgat, G. K.: Absorption spectrum of NO_3 and kinetics of the reactions of NO_3 with NO_2, Cl, and several stable atmospheric species at 298 K, J. Phys. Chem., 89, 4848–4856, https://doi.org/10.1021/j100268a038, 1985.

Cabañas, B., Baeza, M. T., MartÍn, P., Salgado, S., Villanueva, F., Monedero, E., and Wirtz, K.: Products and Mechanism of the NO_3 Reaction with Thiophene, Journal of Atmospheric Chemistry, 51, 317–335, https://doi.org/10.1007/s10874-005-3580-5, 2005.

Cirtog, M., Fouqueau, A., Michoud, V., Cazaunau, M., Bergé, A., Maisonneuve, F., Zapf, P., Pangui, E., Landsheere, X., Giacomoni, J., Gobbi, M., Hannotel, L., Paris, A., Roulier, N., Mellouki, A., Formenti, P., Cantrell, C., Doussin, J.-F., and Picquet-Varralut, B.: Development of a Broad Band Cavity Enhanced Absorption Spectrometer for NO_3 measurements on field and first observations of nighttime NO_3 vertical profiles over Paris, Atmos. Meas. Tech. Discuss., manuscript in preparation.

Claflin, M. S. and Ziemann, P. J.: Identification and Quantitation of Aerosol Products of the Reaction of beta-Pinene with NO_3 Radicals and Implications for Gas- and Particle-Phase Reaction Mechanisms, The Journal of Physical Chemistry A, 122, 3640–3652, https://doi.org/10.1021/acs.jpca.8b00692, pMID: 29528647, 2018.

Crounse, J. D., Nielsen, L. B., Jørgensen, S., Kjaergaard, H. G., and Wennberg, P. O.: Autoxidation of Organic Compounds in the Atmosphere, The Journal of Physical Chemistry Letters, 4, 3513–3520, 2013.

D'Anna, B., Andresen, Ø., Gefen, Z., and Nielsen, C. J.: Kinetic study of OH and NO_3 radical reactions with 14 aliphatic aldehydes, Phys. Chem. Chem. Phys., 3, 3057–3063, https://doi.org/10.1039/B103623H, 2001.

Atmospheric
Measurement
Techniques
Discussions

Dubé, W. P., Brown, S. S., Osthoff, H. D., Nunley, M. R., Ciciora, S. J., Paris, M. W., McLaughlin, R. J., and Ravishankara, A. R.: Aircraft instrument for simultaneous, in situ measurement of NO_3 and N_2O_5 via pulsed cavity ring-down spectroscopy, Review of Scientific Instruments, 77, 34–101, https://doi.org/10.1063/1.2176058, 2006.

Farmer, D. K., Matsunaga, A., Docherty, K. S., Surratt, J. D., Seinfeld, J. H., Ziemann, P. J., and Jimenez, J. L.: Atmospheric Chemistry Special Feature: Response of an aerosol mass spectrometer to organonitrates and organosulfates and implications for atmospheric chemistry, Proceedings of the National Academy of Sciences, 107, 6670–6675, 2010.

Finlayson-Pitts, B. J. and Pitts Jr., J. N.: Chemistry of the Upper and Lower Atmosphere: Theory, Experiments, and Applications, Academic Press, 2000.

Gržinić, G., Bartels-Rausch, T., Berkemeier, T., Türler, A., and Ammann, M.: Viscosity controls humidity dependence of N_2O_5 uptake to citric acid aerosol, Atmospheric Chemistry and Physics, 15, 13 615–13 625, https://doi.org/10.5194/acp-15-13615-2015, 2015.

Hallquist, M., Wängberg, I., Ljungström, E., Barnes, I., and Becker, K.-H.: Aerosol and Product Yields from NO3 Radical-Initiated Oxidation of Selected Monoterpenes, Environ. Sci. Technol., 33, 553–559, https://doi.org/10.1021/es980292s, 1999.

Jenkin, M., Saunders, S., Wagner, V., and Pilling, M.: Protocol for the development of the Master Chemical Mechanism, MCM v3 (Part B): tropospheric degradation of aromatic volatile organic compounds, Atmospheric Chemistry and Physics, 3, 181–193, 2003.

Kang, E., Root, M. J., Toohey, D. W., and Brune, W. H.: Introducing the concept of Potential Aerosol Mass (PAM), Atmospheric Chemistry and Physics, 7, 5727–5744, 2007.

Kennedy, O. J., Ouyang, B., Langridge, J. M., Daniels, M. J. S., Bauguitte, S., Freshwater, R., McLeod, M. W., Ironmonger, C., Sendall, J., Norris, O., Nightingale, R., Ball, S. M., and Jones, R. L.: An aircraft based three channel broadband cavity enhanced absorption spectrometer for simultaneous measurements of NO_3, N_2O_5 and NO_2, Atmospheric Measurement Techniques, 4, 1759–1776, https://doi.org/10.5194/amt-4-1759-2011, 2011.

Knopf, D. A., Forrester, S. M., and Slade, J. H.: Heterogeneous oxidation kinetics of organic biomass burning aerosol surrogates by O3, NO2, N2O5, and NO3, Physical Chemistry Chemical Physics, 13, 21 050, 2011.

Krechmer, J., Lopez-Hilfiker, F., Koss, A., Hutterli, M., Stoermer, C., Deming, B., Kimmel, J., Warneke, C., Holzinger, R., Jayne, J., Worsnop, D., Fuhrer, K., Gonin, M., and de Gouw, J.: Evaluation of a New Reagent-Ion Source and Focusing Ion–Molecule Reactor for Use in Proton-Transfer-Reaction Mass Spectrometry, Analytical Chemistry, 90, 12 011–12 018, https://doi.org/10.1021/acs.analchem.8b02641, pMID: 30220198, 2018.

Lambe, A. T., Ahern, A. T., Williams, L. R., Slowik, J. G., Wong, J. P. S., Abbatt, J. P. D., Brune, W. H., Ng, N. L., Wright, J. P., Croasdale, D. R., Worsnop, D. R., Davidovits, P., and Onasch, T. B.: Characterization of aerosol photooxidation flow reactors: heterogeneous oxidation, secondary organic aerosol formation and cloud condensation nuclei activity measurements, Atmospheric Measurement Techniques, 4, 445–461, 2011.

Lambe, A. T., Chhabra, P. S., Onasch, T. B., Brune, W. H., Hunter, J. F., Kroll, J. H., Cummings, M. J., Brogan, J. F., Parmar, Y., Worsnop, D. R., Kolb, C. E., and Davidovits, P.: Effect of oxidant concentration, exposure time, and seed particles on secondary organic aerosol chemical composition and yield, Atmospheric Chemistry and Physics, 15, 3063–3075, 2015.

Lambe, A. T., Massoli, P., Zhang, X., Canagaratna, M. R., Nowak, J. B., Daube, C., Yan, C., Nie, W., Onasch, T. B., Jayne, J. T., Kolb, C. E., Davidovits, P., Worsnop, D. R., and Brune, W. H.: Controlled nitric oxide production via $O(^1D) + N_2O$ reactions for use in oxidation flow reactor studies, Atmospheric Measurement Techniques, 10, 2283–2298, https://doi.org/10.5194/amt-10-2283-2017, 2017.

Atmospheric
Measurement
Techniques
Discussions

Lambe, A. T., Krechmer, J. E., Peng, Z., Casar, J. R., Carrasquillo, A. J., Raff, J. D., Jimenez, J. L., and Worsnop, D. R.: HO_x and NO_x production in oxidation flow reactors via photolysis of isopropyl nitrite, isopropyl nitrite-d$_7$, and 1,3-propyl dinitrite at $\lambda = 254$, 350, and 369 nm, Atmospheric Measurement Techniques, 12, 299–311, https://doi.org/10.5194/amt-12-299-2019, 2019.

Langridge, J. M., Ball, S. M., Shillings, A. J. L., and Jones, R. L.: A broadband absorption spectrometer using light emitting diodes for ultrasensitive, in situ trace gas detection, Review of Scientific Instruments, 79, 123 110, https://doi.org/10.1063/1.3046282, 2008.

Lee, B. H., Lopez-Hilfiker, F. D., Mohr, C., Kurten, T., Worsnop, D. R., and Thornton, J. A.: An Iodide-Adduct High-Resolution Time-of-Flight Chemical-Ionization Mass Spectrometer: Application to Atmospheric Inorganic and Organic Compounds, Environmental Science and Technology, 48, 6309–6317, 2014.

Li, R., Palm, B. B., Ortega, A. M., Hlywiak, J., Hu, W., Peng, Z., Day, D. A., Knote, C., Brune, W. H., De Gouw, J. A., and Jimenez, J. L.: Modeling the Radical Chemistry in an Oxidation Flow Reactor: Radical Formation and Recycling, Sensitivities, and the OH Exposure Estimation Equation, The Journal of Physical Chemistry A, 119, 150406123535 006, 2015.

Manion, J. A., Huie, R. E., Levin, R. D., Jr., D. R. B., Orkin, V. L., Tsang, W., McGivern, W. S., Hudgens, J. W., Knyazev, V. D., Atkinson, D. B., Chai, E., Tereza, A. M., Lin, C.-Y., Allison, T. C., Mallard, W. G., Westley, F., Herron, J. T., Hampson, R. F., , and Frizzell, D. H.: NIST Chemical Kinetics Database, NIST Standard Reference Database 17, Version 7.0 (Web Version), Release 1.6.8, Data version 2015.09, Tech. rep., National Institute of Standards and Technology, Gaithersburg, Maryland, http://kinetics.nist.gov/, 2015.

Melaas, E. K., Wang, J. A., Miller, D. L., and Friedl, M. A.: Interactions between urban vegetation and surface urban heat islands: a case study in the Boston metropolitan region, Environmental Research Letters, 11, 054 020, https://doi.org/10.1088/1748-9326/11/5/054020, 2016.

Middlebrook, A. M., Bahreini, R., Jimenez, J. L., and Canagaratna, M. R.: Evaluation of Composition-Dependent Collection Efficiencies for the Aerodyne Aerosol Mass Spectrometer using Field Data, Aerosol Science and Technology, 46, 258–271, 2012.

Ng, N. L., Brown, S. S., Archibald, A. T., Atlas, E., Cohen, R. C., Crowley, J. N., Day, D. A., Donahue, N. M., Fry, J. L., Fuchs, H., Griffin, R. J., Guzman, M. I., Herrmann, H., Hodzic, A., Iinuma, Y., Jimenez, J. L., Kiendler-Scharr, A., Lee, B. H., Luecken, D. J., Mao, J., McLaren, R., Mutzel, A., Osthoff, H. D., Ouyang, B., Picquet-Varrault, B., Platt, U., Pye, H. O. T., Rudich, Y., Schwantes, R. H., Shiraiwa, M., Stutz, J., Thornton, J. A., Tilgner, A., Williams, B. J., and Zaveri, R. A.: Nitrate radicals and biogenic volatile organic compounds: oxidation, mechanisms, and organic aerosol, Atmospheric Chemistry and Physics, 17, 2103–2162, https://doi.org/10.5194/acp-17-2103-2017, 2017.

Orlando, J. J. and Tyndall, G. S.: Laboratory studies of organic peroxy radical chemistry: an overview with emphasis on recent issues of atmospheric significance, Chem. Soc. Rev., 41, 6294–6317, https://doi.org/10.1039/C2CS35166H, 2012.

Orphal, J., Fellows, C. E., and Flaud, P.-M.: The visible absorption spectrum of NO3 measured by high-resolution Fourier transform spectroscopy, Journal of Geophysical Research: Atmospheres, 108, https://doi.org/10.1029/2002JD002489, 2003.

Palm, B. B., Campuzano-Jost, P., Day, D. A., Ortega, A. M., Fry, J. L., Brown, S. S., Zarzana, K. J., Dube, W., Wagner, N. L., Draper, D. C., Kaser, L., Jud, W., Karl, T., Hansel, A., Gutiérrez-Montes, C., and Jimenez, J. L.: Secondary organic aerosol formation from in situ OH, O_3, and NO_3 oxidation of ambient forest air in an oxidation flow reactor, Atmospheric Chemistry and Physics, 17, 5331–5354, https://doi.org/10.5194/acp-17-5331-2017, 2017.

Peng, Z. and Jimenez, J. L.: Modeling of the chemistry in oxidation flow reactors with high initial NO, Atmospheric Chemistry and Physics, 17, 11 991–12 010, https://doi.org/10.5194/acp-17-11991-2017, 2017.

Peng, Z. and Jimenez, J. L.: KinSim: A Research-Grade, User-Friendly, Visual Kinetics Simulator for Chemical-Kinetics and Environmental-Chemistry Teaching, J. Chem. Educ., 96, 806–811, https://doi.org/10.1021/acs.jchemed.9b00033, 2019.

Atmospheric
Measurement
Techniques
Discussions

Peng, Z., Day, D. A., Stark, H., Li, R., Lee-Taylor, J., Palm, B. B., Brune, W. H., and Jimenez, J. L.: HO_x radical chemistry in oxidation flow reactors with low-pressure mercury lamps systematically examined by modeling, Atmospheric Measurement Techniques, 8, 4863–4890, 2015.

Peng, Z., Palm, B. B., Day, D. A., Talukdar, R. K., Hu, W., Lambe, A. T., Brune, W. H., and Jimenez, J. L.: Model Evaluation of New
5 Techniques for Maintaining High-NO Conditions in Oxidation Flow Reactors for the Study of OH-Initiated Atmospheric Chemistry, ACS Earth Space Chem., 2, 72–86, https://doi.org/10.1021/acsearthspacechem.7b00070, 2018.

Peng, Z., Lee-Taylor, J., Orlando, J. J., Tyndall, G. S., and Jimenez, J. L.: Organic peroxy radical chemistry in oxidation flow reactors and environmental chambers and their atmospheric relevance, Atmospheric Chemistry and Physics, 19, 813–834, https://doi.org/10.5194/acp-19-813-2019, 2019.

10 Platz, J., Nielsen, O. J., Wallington, T. J., Ball, J. C., Hurley, M. D., Straccia, A. M., Schneider, W. F., and Sehested, J.: Atmospheric Chemistry of the Phenoxy Radical, C_6H_5O: UV Spectrum and Kinetics of its Reaction with NO, NO_2 and O_2, J. Phys. Chem. A, 102, 7964–7974, https://doi.org/10.1021/jp982221l, 1998.

Romanini, D., Kachanov, A., Sadeghi, N., and Stoeckel, F.: CW cavity ring down spectroscopy, Chemical Physics Letters, 264, 316 – 322, https://doi.org/https://doi.org/10.1016/S0009-2614(96)01351-6, 1997.

15 Saunders, S., Jenkin, M., Derwent, R., and Pilling, M.: Protocol for the development of the Master Chemical Mechanism, MCM v3 (Part A): tropospheric degradation of non-aromatic volatile organic compounds, Atmospheric Chemistry and Physics, 3, 161–180, 2003.

Short, K. C.: Spatial wildfire occurrence data for the United States, 1992-2015, 4th Edition, https://doi.org/https://doi.org/10.2737/RDS-2013-0009.4, 2017.

Stutz, J., Alicke, B., Ackermann, R., Geyer, A., White, A., and Williams, E.: Vertical profiles of NO3, N2O5, O3, and NOx in the nocturnal
20 boundary layer: 1. Observations during the Texas Air Quality Study 2000, J. Geophys. Res., 109, https://doi.org/10.1029/2003jd004209, 2004.

Vandaele, A. C., Hermans, C., Simon, P. C., Carleer, M., Colin, R., Fally, S., Mérienne, M. F., Jenouvrier, A., and Coquart, B.: Measurements of the NO_2 absorption cross-section from 42,000 cm^{-1} to 10,000 cm^{-1} (238-1000 nm) at 220 K and 294 K., J. Quant. Spectrosc. Radiat. Transf., 59, 171–184, https://doi.org/10.1016/S0022-4073(97)00168-4, 1998.

25 Venables, D. S., Gherman, T., Orphal, J., Wenger, J. C., and Ruth, A. A.: High Sensitivity in Situ Monitoring of NO_3 in an Atmospheric Simulation Chamber Using Incoherent Broadband Cavity-Enhanced Absorption Spectroscopy, Environ. Sci. Technol., 40, 6758–6763, https://doi.org/10.1021/es061076j, 2006.

Wagner, C., Hanisch, F., Holmes, N., de Coninck, H., Schuster, G., and Crowley, J. N.: The interaction of N_2O_5 with mineral dust: aerosol flow tube and Knudsen reactor studies, Atmospheric Chemistry and Physics, 8, 91–109, https://doi.org/10.5194/acp-8-91-2008, https:
30 //www.atmos-chem-phys.net/8/91/2008/, 2008.

Warneck, P. and Williams, J.: The Atmospheric Chemist's Companion, Springer, Dordrecht, https://doi.org/https://doi.org/10.1007/978-94-007-2275-0, 2012.

Wayne, R. P., Barnes, I., Biggs, P., Burrows, J. P., Canosa-Mas, C. E., Hjorth, J., Le Bras, G., Moortgat, G. K., Perner, D., Poulet, G., Restelli, G., and Sidebottom, H.: The nitrate radical: physics, chemistry, and the atmosphere, Atmospheric Environment, Part A: General Topics,
35 25, 1–203, 1991.

Wood, E. C., Wooldridge, P. J., Freese, J. H., Albrecht, T., and Cohen, R. C.: Prototype for In Situ Detection of Atmospheric NO_3 and N_2O_5 via Laser-Induced Fluorescence, Environmental Science & Technology, 37, 5732–5738, https://doi.org/10.1021/es034507w, pMID: 14717187, 2003.

Xu, W., Lambe, A., Silva, P., Hu, W., Onasch, T., Williams, L., Croteau, P., Zhang, X., Renbaum-Wolff, L., Fortner, E., Jimenez, J. L., Jayne, J., Worsnop, D., and Canagaratna, M.: Laboratory evaluation of species-dependent relative ionization efficiencies in the Aerodyne Aerosol Mass Spectrometer, Aerosol Science and Technology, 52, 626–641, https://doi.org/10.1080/02786826.2018.1439570, 2018.

Table 1. Fit parameters for NO_{3exp} estimation equation (Equation 5).

Parameter	Subspace 1 Values	Subspace 2 Values	Subspace 3 Values
a	61.0694	-59.3835	246.416
b	-20.1400	27.3434	-122.229
c	0.795209	0.803508	0.581443
d	-0.375825	1.18285	51.2355
e	0.0311034	0.00815681	-0.66569
f	0.888193	-0.0731138	-0.0210958
g	-0.379009	0.13199	-0.346062
h	1.73605	-0.422009	-81.9221
i	0.14737	0.035132	-22.4373
j	0.261402	0.311104	13.204
k	-1.22009	-0.323329	-0.118988
l	0.00733645	-0.004277	0.676436
m	-0.957064	-0.436977	-0.3983
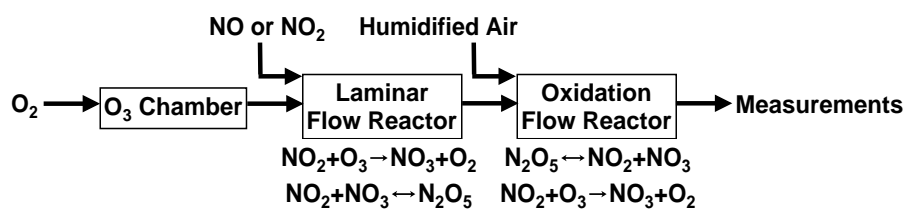
Figure 1. Process flow diagram of the OFR-iN$_2$O$_5$ technique used to generate nitrate radicals (NO$_3$).

Atmospheric
Measurement
Techniques
Discussions

Open Access

EGU
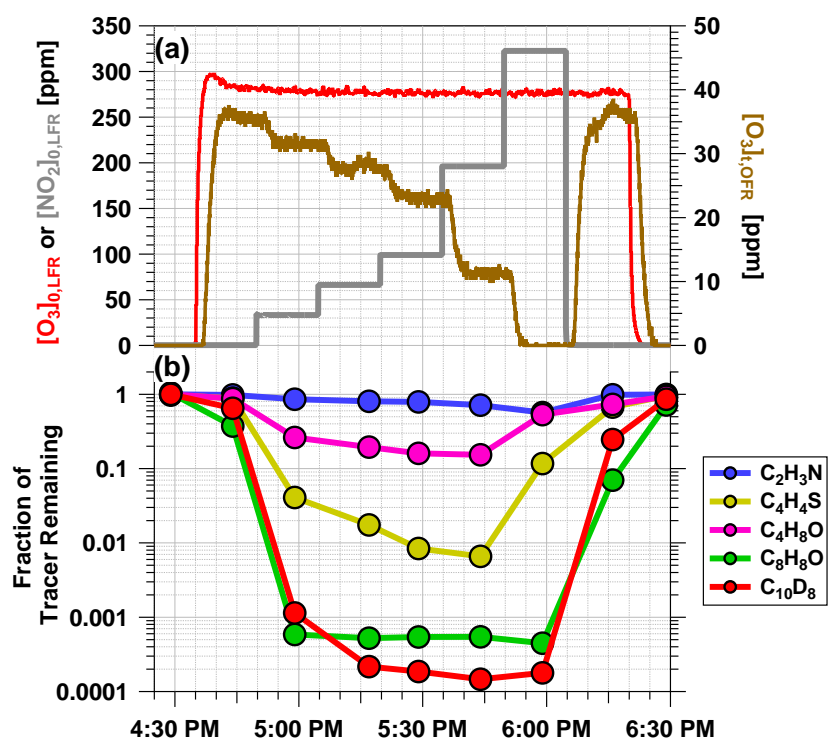
Figure 2. Time series from a representative OFR-iN_2O_5 characterization experiment conducted at RH_{OFR} = 11% of (a) O_3 and NO_2 mixing ratios input to LFR (left axis) and O_3 measured at the exit of the OFR (right axis) (b) VOC tracers measured with PTR-MS: acetonitrile (C_2H_3N), butanal (C_4H_8O), thiophene (C_4H_4S), 2,3-dihydrobenzofuran (C_8H_8O) and naphthalene-d$_8$ ($C_{10}D_8$).

Atmospheric
Measurement
Techniques
Discussions
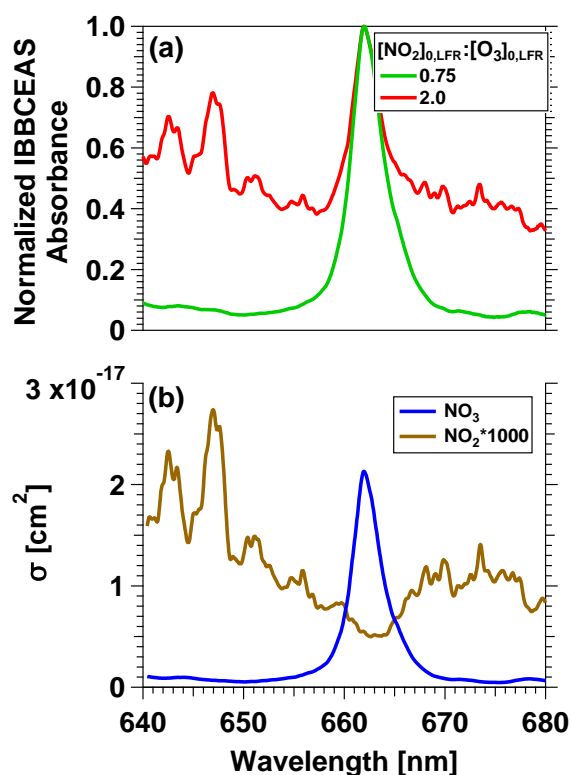
Figure 3. (a) IBBCEAS measurements of NO_2 and NO_3 absorbance obtained from an OFR-iN_2O_5 characterization experiment conducted at $[O_3]_{0,LFR}$ = 150-160 ppm and $[NO_2]_{0,LFR}$:$[O_3]_{0,LFR}$ = 0.75 and 2.0. (b) Absorption cross sections of NO_2 and NO_3 (Vandaele et al., 1998; Orphal et al., 2003).
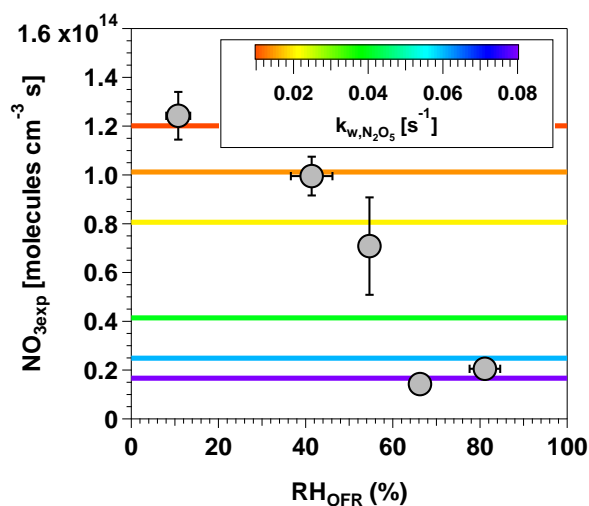
Figure 4. NO_{3exp} as a function of RH_{OFR} at $[O_3]_{0,LFR} = 250$ ppm and $[NO_2]_{0,LFR} = 130$ ppm. Horizontal lines represent N_2O_5 wall loss rate constants ranging from 0.01 to 0.08 s^{-1} that were input to the OFR-iN_2O_5 KinSim mechanism (Table S2).
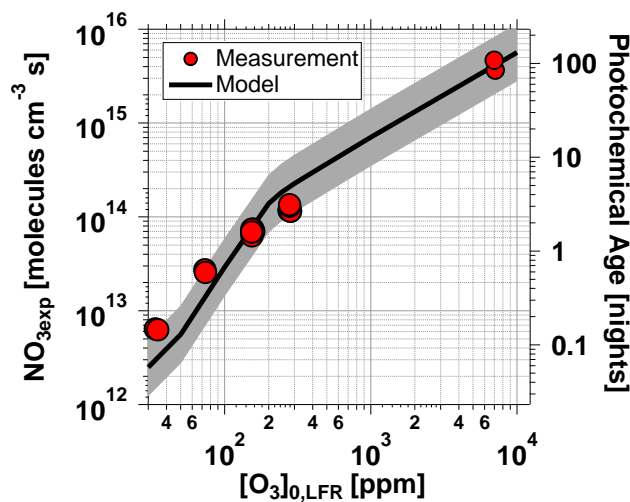
Figure 5. NO_{3exp} as a function of $[O_3]_{0,LFR}$ for measurements with $[NO_2]_{0,LFR}:[O_3]_{0,LFR} = 0.5 \pm 0.1$. Equivalent ambient photochemical age was calculated assuming a 14-hour average nighttime NO_3 mixing ratio of 30 ppt and 10-hour daytime average NO_3 mixing ratio of 0 ppt (Asaf et al., 2010). Model inputs: $k_{w,N_2O_5} = 0.01$ s^{-1} and $NO_3R_{ext} = 0.07$ s^{-1} ($[O_3]_{0,LFR} < 1000$ ppm) or 0.38 s^{-1} ($[O_3]_{0,LFR} > 1000$ ppm). Shaded region encompasses model output scaled by factors of 0.5 and 2.
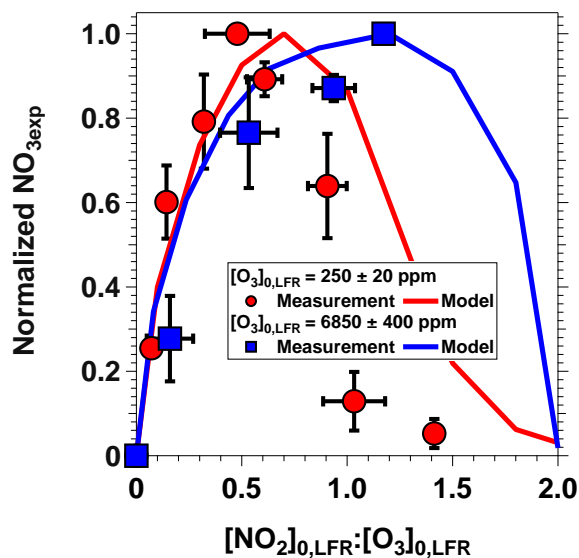
Figure 6. NO_{3exp} as a function of $[NO_2]_{0,LFR}:[O_3]_{0,LFR}$ at fixed $[O_3]_{0,LFR}$ values of 250 ± 20 and 6850 ± 400 ppm and $RH_{OFR} = 11\%$ to 81%. NO_{3exp} values were normalized to maximum NO_{3exp} value obtained at the same RH.
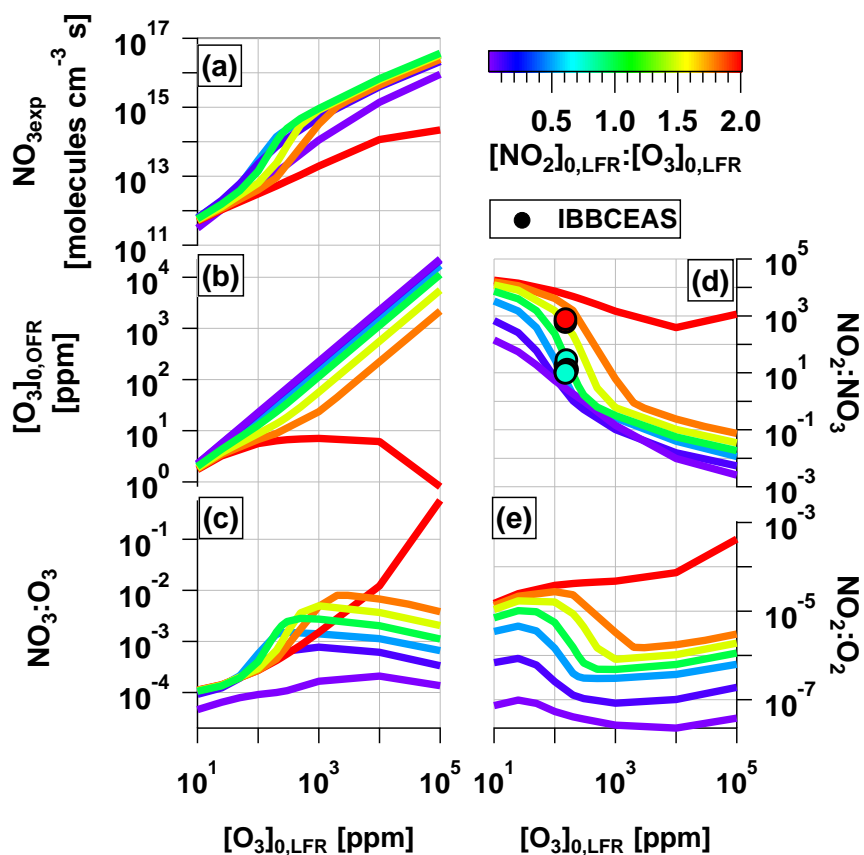
Figure 7. Modeled (a) NO_{3exp}, (b) $[O_3]$, (c) $NO_3{:}O_3$, (d) $NO_2{:}NO_3$, and (e) $NO_2{:}O_2$ as a function of $[O_3]_{0,LFR} = 10$ ppm to 10^5 ppm, for $[NO_2]_{0,LFR}{:}[O_3]_{0,LFR} = 0.01, 0.1, 0.5, 1.0, 1.5, 1.8$ and 2.0. Model inputs: $k_{w,N_2O_5} = 0.01$ s^{-1}, $NO_3R_{ext} = 0.07$ s^{-1}. IBBCEAS-measurd $NO_2{:}NO_3$ values are plotted in (d).
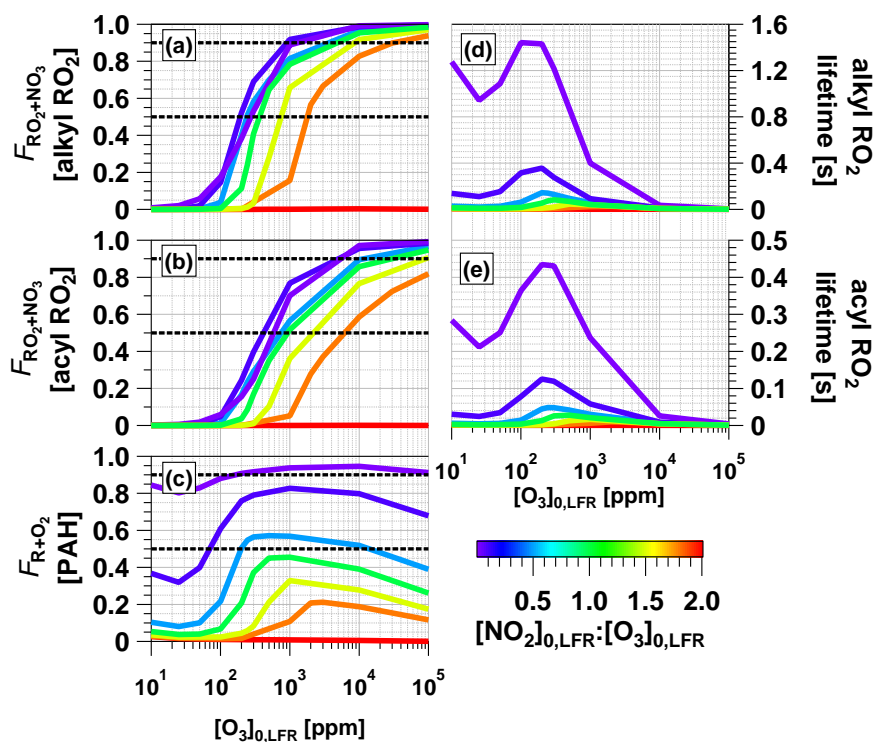
Figure 8. $F_{RO_2+NO_3}$ for (a) alkyl and (b) acyl RO_2, and (c) F_{R+O_2} over the same OFR-iN$_2$O$_5$ operating conditions and model inputs used to generate Figure 7, with corresponding lifetimes for (d) alkyl and (e) acyl RO_2.
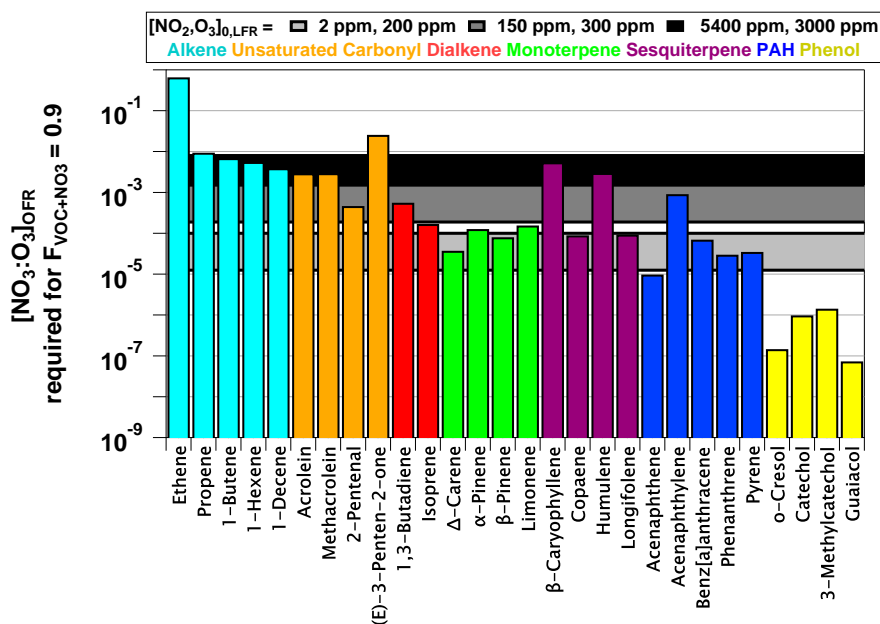
Figure 9. $NO_3{:}O_3$ at which $F_{VOC+NO_3} = 0.9$ for representative VOCs with $k_{NO_3} > 10^{-16}$ and $k_{O_3} > 10^{-19}$ cm^3 molecules^{-1} s^{-1} (Manion et al., 2015). Horizontal bands represent upper and lower limit values calculated assuming $k_{w,N_2O_5} = 0.01$ and 0.08 s^{-1}.
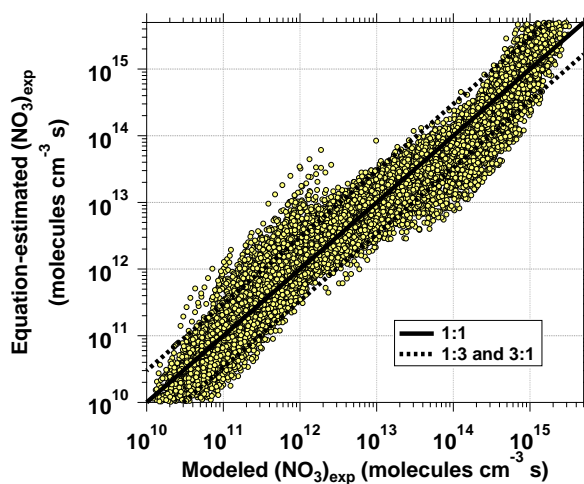
Figure 10. NO_{3exp} calculated from estimation equation (Equation 5 and Table 1) as a function of NO_{3exp} calculated from full OFR-iN$_2$O$_5$ KinSim mechanism (Table S2). Solid and dashed lines correspond to 1:1, 1:3 and 3:1 lines respectively.

Atmospheric
Measurement
Techniques
Open Access
EGU
Discussions
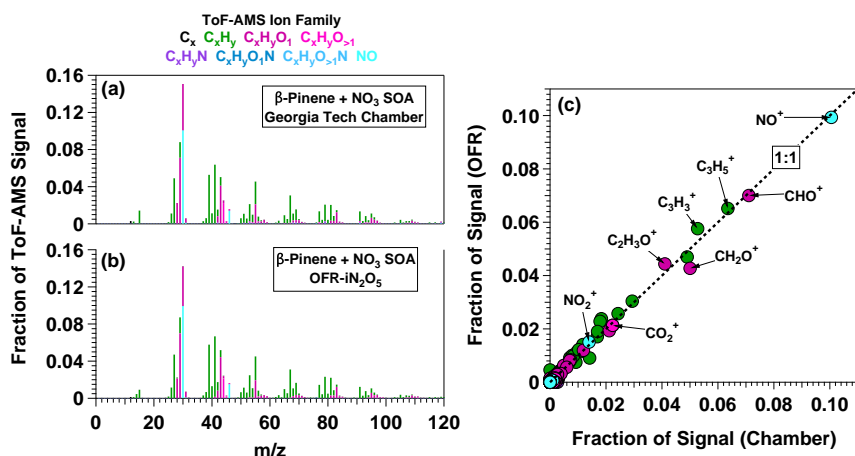
Figure 11. AMS spectra of SOA generated from NO_3 oxidation of β-pinene in (a) Georgia Tech environmental chamber (Boyd et al., 2015) and (b) OFR-iN_2O_5. Scatter plot in (c) shows spectra generated in the OFR and chamber plotted against each other.
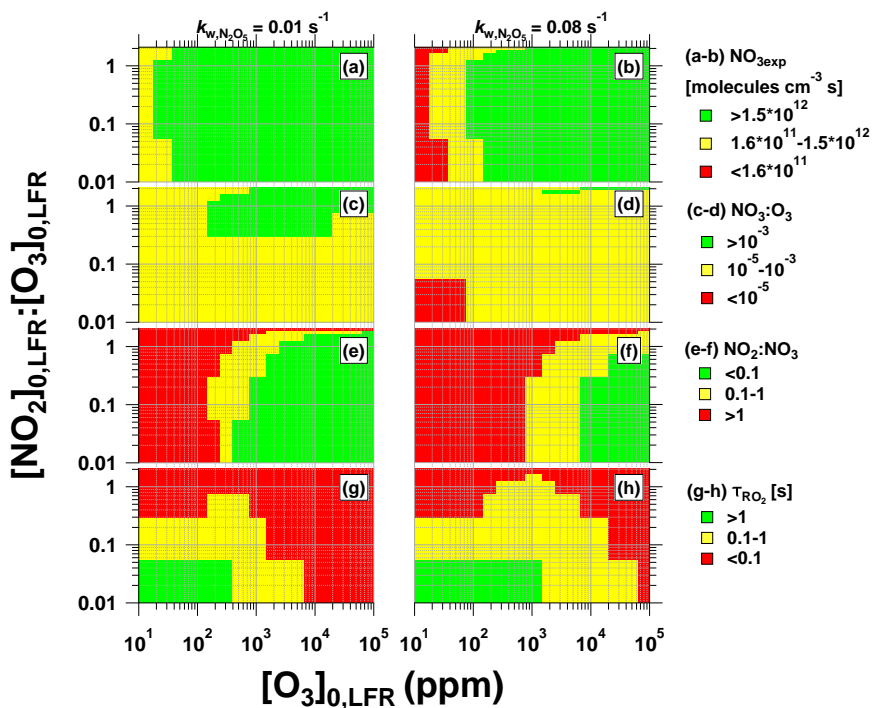
Figure 12. Summary of OFR-iN_2O_5 operating conditions suitable for maximum (a-b) NO_3exp, (c-d) NO_3:O_3, (e-f) NO_2:NO_3, and (g-h) τ_{RO_2} assuming k_{w,N_2O_5} = 0.01 and 0.08 s^{-1}.